Combustion and Flame 162 (2015) 2569–2581

Contents lists available at ScienceDirect

Combustion and Flame

journal homepage: www.elsevier.com/locate/combustflame

Numerical simulation and parametric sensitivity study of particle size distributions in a burner-stabilised stagnation flame

Edward K.Y. Yapp [a], Dongping Chen [a], Jethro Akroyd [a], Sebastian Mosbach [a], Markus Kraft [a,b,*], Joaquin Camacho [c], Hai Wang [c]

[a] Department of Chemical Engineering and Biotechnology, University of Cambridge, New Museums Site, Pembroke Street, Cambridge CB2 3RA, United Kingdom
[b] School of Chemical and Biomedical Engineering, Nanyang Technological University, 62 Nanyang Drive, Singapore 637459, Singapore
[c] Department of Mechanical Engineering, Stanford University, Stanford, CA 94305, United States

ARTICLE INFO

Article history:
Received 10 February 2015
Received in revised form 6 March 2015
Accepted 9 March 2015
Available online 26 March 2015

Keywords:
Soot
Particle size distribution
Premixed flame
Numerical simulation
Parametric sensitivity study
PAH

ABSTRACT

A detailed population balance model is used to perform a parametric sensitivity study on the computed particle size distributions (PSDs) for a laminar premixed ethylene burner-stabilised stagnation flame. The soot morphology in the post-flame region is studied using computed sintering level distributions, fringe length analysis of the polycyclic aromatic hydrocarbons (PAHs) within the primary soot particles, and TEM-like projections of aggregates. The computed PSDs were sensitive to the minimum particle inception size, the coagulation rate and the inception species concentration. Changes in the particle inception size and the coagulation rate led to an overall shift in the position of the coagulation peak. Only changes in the inception species concentration led to a systematic shift in both the position of the trough between the modes of the bimodal PSD and the coagulation peak at larger diameters. Given the overall model, varying the inception species concentration with each burner-stagnation plate separation was the only means possible to achieve a satisfactory agreement between the experimental and computed PSDs. This study shows that further work is required to better understand the soot precursor chemistry, the inception of soot particles. Additional work may also be needed in the area of experimental mobility sizing for the flame studied here.

1. Introduction

Much progress has been made to understand the chemical and physical processes underlying soot formation. However, details of the individual processes remain an open question [1,2]. In general, a basic understanding of the complex and often competitive processes of soot nucleation and mass/size growth requires detailed kinetic modeling through comparison of model results and experimental data and sensitivity analysis. For this purpose, a range of experimental techniques have been developed to probe the size and mass evolution of soot in flames. Soot volume fraction is most commonly measured using light extinction and scattering [3] and laser light incandescence [4]. However, interpretation of the laser-based experiment requires a fairly precise knowledge about the refractive index of young soot which remains poorly understood. In principle, independent verification of the optical measurements may be made using small-angle neutron scattering [5], small-angle X-ray scattering [6] and thermocouple particle densitometry [7], though very little systematic efforts have been made in that direction. The detailed distribution of particle sizes may be measured by a scanning mobility particle sizer (SMPS) (see, e.g., [8–13]). Though the method is intrusive to the flame, it nonetheless provides more detailed features about the evolution of the particle size distribution (PSD), from very small, incipient particles to aggregates as large as 100 nm in mobility diameter. Ex situ analysis by high-resolution microcopy of particles collected by a rapid insertion technique has been routinely employed (see, e.g., [14–17]). Whilst transmission electron microscopy (TEM) images show the morphology of a soot particle, the higher magnification (see, e.g., [18]) is able to reveal some details of the internal structure of mature soot. Imaging incipient soot a few nanometers in size by TEM is challenging [10], because of potential sample damage by the vacuum environment and the high-energy electron beam of TEM, as shown recently by Schenk et al. [17]. Recent advances in Helium ion microscopy (HIM) [17,19] offer a

* Corresponding author at: Department of Chemical Engineering and Biotechnology, University of Cambridge, New Museums Site, Pembroke Street, Cambridge CB2 3RA, United Kingdom. Fax: +44 1223 334796.
E-mail addresses: mk306@cam.ac.uk (M. Kraft), haiwang@stanford.edu (H. Wang).
URL: http://como.cheng.cam.ac.uk (M. Kraft).

http://dx.doi.org/10.1016/j.combustflame.2015.03.006
0010-2180/

low-energy, softer and high-contrast solution to incipient soot imaging. The chemical composition of soot may be analysed using laser microprobe spectroscopy [14,20] and photoionisation aerosol mass spectroscopy [21].

A large portion of the experimental data that are available with regards to the time evolution of soot PSD has been gathered in premixed flames [8–10,13,21–24]. A sample probe is typically placed across the flame and PSDs would be measured by a SMPS. This sampling technique is inherently intrusive and perturbs the flame [8,25]. For this reason, a premixed burner-stabilised stagnation flame (BSSF) configuration was introduced where the sample probe is integrated into a water-cooled stagnation plate as a flow stagnation surface for which pseudo-one-dimensional numerical solution of the flame problem becomes feasible [26]. The probe in that setup may be treated as the flame boundary condition; thus, eliminating the problem in earlier setups in which the probe effects on fluid mechanics and reaction kinetics cannot be quantified easily. The setup, along with the numerical modeling method for such flames, removes the need to carry out arbitrary "time or spatial distance shifting" as it was customarily employed in comparison of experimental data and modelling result.

Beyond the probe effect, measurements by SMPS coupled with BSSF faces other complications when such measurements are used for testing models. Like any other techniques for probing soot in flames, the interpretation of the data is not always straightforward. Mobility measurements yields essentially the collision diameter of the particles. Thus two factors can impact a proper comparison between model and experiment. The first factor lies in the unknown morphology of the particles undergoing mass and size growth. The second factor is related to the internal structure of the particles and thus the mass density of the particle. HIM measurements have shown that particles < 10 nm in size can exhibit odd, non-spherical shapes [17,19]. Considering the experimental issues just discussed, it would be beneficial to carry out a study in which the model and experimental uncertainties are considered sequentially. This paper will be a step in that direction.

The soot PSDs for an ethylene BSSF were modelled by Lindstedt and Waldheim [27] using a surface-volume description of particles and a sectional method. To counteract the excessive depletion of the small particles in their model, they introduced a collision efficiency for coagulation which varies between 1 for particle diameters greater than 5 nm and about 0.01 for pyrene. However, there are still some unresolved problems. For example, the model is unable to predict particle diameters across all burner-stagnation plate separations. It remains unclear whether the discrepancy is caused by the particle morphological assumptions of the model in the simulation or by other factors.

There are also many detailed models of soot formation and solution methods. For example, Kraft and co-workers [28–34] employ a detailed population balance model which is solved using a stochastic method. The model describes particles as aggregates composed of primary particles which are in turn composed of individual polycyclic aromatic hydrocarbons (PAHs), thus containing information on particle size, morphology, and the internal structure of nanoparticles. This particular modelling approach has been successfully applied to the analysis of a variety of nanoparticles. It was used to simulate the PSDs of soot particles in laminar premixed flames [22,35,36] and to uncover the various factors that govern the shape of PSDs and their time evolution [22,35]. Specifically, Singh et al. [35] performed a sensitivity analysis of the PSDs to various kinetic parameters in the hydrogen-abstraction–carbon addition (HACA) mechanism [37]. A unique feature of the model is that it resolves the size and connectivity of the primary particles in an aggregate; therefore, TEM-like projections of aggregates could be produced to visualise the temporal evolution of the fractal dimension in different flames [36]. Similar investigations of soot PSDs, morphology and composition have been performed in the context of engines [38]. The stochastic approach was also used to follow the morphology of aerosols in Titan's atmosphere [39] and to study the sintering of titania [40], silica [41] and silicon [42]. One has to be aware, though, that the increasing complexity of the model comes at a cost of including a large number of parameters, some of which were calibrated against experiments, while others remain poorly known.

The **purpose of this paper** is to investigate whether the model can describe the evolution of soot PSDs observed in the BSSF of [26]. The flame chemistry and structure was computed using a pseudo-one-dimensional stagnation flow flame code with appropriate boundary conditions. The particle dynamics were solved using a detailed population balance model. A thorough parametric sensitivity study is carried out here to understand how the various submodels and model parameters impact the various PSD features quantitatively and to shed light on the mobility measurement, especially concerning the particle morphology and its effect on the interpretation of the mobility diameter.

The paper is organised as follows: Section 2 introduces the gas-phase chemical mechanism, the governing equations and boundary conditions for the burner-stagnation flame configuration, and key aspects of the detailed population balance model. Sections 3.1 and 3.2 present the temperature and species profiles, and the PSDs. Section 3.3 presents the parametric sensitivity study of the computed PSDs. Section 3.4 shows various aspects of the soot morphology calculated from the detailed population balance model. Lastly, implications on the experimental measurements are discussed in Section 4.

2. Computational method

The computational method consists of two parts. In the first part, temperature and species profiles are computed using a modified version [26] of Oppdif [43,44], including calculation of the source terms by the Method of Moment with Interpolative Closure (MOMIC) using the code published by Revzan et al. [45]. A gas-phase chemical mechanism, and species thermodynamic and transport properties are supplied as input. The transport equations of the moments of the PSD are solved to approximately account for the production and consumption of key gas-phase species due to inception, surface growth, oxidation and condensation processes. A total of six moments, including the zeroth moment, were solved using MOMIC to close the moment transport equations. In the second part, a detailed population balance model is applied as a post-processing step where the computed temperature and species profiles from Oppdif are supplied as input. This two-step methodology has been applied to the studies of a number of laminar premixed flames [46–48] and ideal reactor simulations [49].

Oppdif simulations were performed using an unburned-gas composition (molar basis) of 16.3% ethylene, 23.7% oxygen and 60% argon (an equivalence ratio of 2.07), a cold-gas velocity of 8 cm/s (STP), a gas temperature of 473 K at the burner surface and at atmospheric pressure. The method for determining the gas temperature at the burner surface has been discussed in [26]. Windward differencing was used and multi-component transport and thermal diffusion were considered. About 200 grid points were found to be sufficient for convergence. The energy equation was solved with both gas and particle radiation.

The detailed population balance model requires the computed profiles from Oppdif to be expressed in terms of the residence time of a Lagrangian particle travelling from the burner to the stagnation plate. The combined axial convective velocity and thermophoretic velocity were used to perform the conversion as per Abid et al. [26].

2.1. Gas-phase chemistry

The ABF mechanism [50] as supplied with the Chemkin-Pro installation package [51] was used to describe the gas-phase chemistry. The reaction mechanism is an extension of the model described in Wang and Frenklach [52], which includes combustion chemistry and the formation and growth pathways of PAHs up to pyrene [52], and additional PAH growth reactions added by Appel et al. [50].

2.2. Governing equations and boundary conditions

The BSSF configuration is shown in Fig. 1. By assuming that the radial velocity varies linearly in the radial direction, the governing equations for the 2D axisymmetric flow field may be reduced to a set of 1D equations [44,53,54]. The energy and moment transport equations are stated here while the continuity, radial momentum, radial pressure gradient eigenvalue and species equations may be found in [53]. For ease of reference the notation used here was chosen to be consistent with [53].

Energy equation

$$2U\frac{\mathrm{d}T}{\mathrm{d}z}-\frac{1}{c_p}\frac{\mathrm{d}}{\mathrm{d}z}\left(\lambda\frac{\mathrm{d}T}{\mathrm{d}z}\right)+\frac{\rho}{c_p}\sum_{k=1}^{N}c_{p,k}Y_kV_k\frac{\mathrm{d}T}{\mathrm{d}z}+\frac{1}{c_p}\sum_{k=1}^{N}h_k\dot{\omega}_k+\frac{1}{c_p}\dot{Q}_{\mathrm{rad}}=0, \tag{1}$$

where U is a variable related to the axial velocity, T is the temperature, z is the axial distance, c_p is the specific heat capacity at constant pressure of the mixture, λ is the thermal conductivity, ρ is the density and N is the number gas-phase species. $c_{p,k}$ is the specific heat capacity at constant pressure, Y_k is the mass fraction, V_k is the multicomponent diffusion velocity, h_k is the molar enthalpy and $\dot{\omega}_k$ is the molar chemical rate of production per unit volume of the k-th gas-phase species.

The gas radiation heat loss term in [26] was extended to include the contribution from the particle phase [55]:

$$\dot{Q}_{\mathrm{rad}}=4\sigma(T^4-T_{\mathrm{amb}}^4)\left(\sum_{k}^{N}p(X_ka_k)+\kappa_{\mathrm{particle}}\right), \tag{2}$$

where σ is the Stefan–Boltzmann constant, T_{amb} is the ambient temperature taken to be the average of the burner and stagnation plate temperatures [26], p is the pressure, X_k is the mole fraction of the k-th gas-phase species, and a_k and κ are the Planck mean absorption coefficients of the k-th gas-phase species and soot particle, respectively. The Planck mean absorption coefficient of the particle may be expressed as [56,57]:

$$\kappa_{\mathrm{particle}}=3.83f_vC_0T/C_2,\quad C_0=\frac{36\pi nk}{(n^2-k^2+2)^2+4n^2k^2}, \tag{3}$$

where f_v is the soot volume fraction. $C_0=4.8922$ (dimensionless) is a constant depending on the complex refractive index of soot, where $n=1.57$ and $k=0.56$ are the refractive and absorptive indices, respectively [58]. $C_2=1.4388$ cm K is the second Planck function constant. Or more commonly the refractive index absorption function $E(m)$ is 0.26. Values of around 0.4 for mature soot have been reported in the literature (see, e.g., [59]) which is about two times the value used in this work. However, as argued in [26], for the current set of lightly sooting flames the mean absorption coefficient of soot is two orders of magnitude lower than that for gas radiating species. Therefore, a larger value of $E(m)$ of 0.4 will only have a negligible impact on the radiation heat loss term and consequently the temperature predictions.

Moment transport equation

$$2U\frac{\partial}{\partial z}\left(\frac{M_r}{\rho}\right)-\frac{\partial}{\partial z}\left[\rho D_{p,1}\frac{\partial}{\partial z}\left(\frac{M_{r-2/3}}{\rho}\right)\right]+\frac{\partial v_TM_r}{\partial z}-\dot{M}_r=0,\quad r=0,\ldots,\infty, \tag{4}$$

where the moments of the size distribution of particles are defined as [60]:

$$M_r=\sum_{i=1}^{\infty}i^rN_i,\quad r=0,\ldots,\infty. \tag{5}$$

The $\dot{M}_r$ term in Eq. (4) is the moment source term as contributed by inception, coagulation, surface growth, oxidation and condensation [60–62]. In the ABF model, the growth of PAHs is carried out to infinity, the binary collision of any two PAH species after pyrene was assumed as particle nucleation, and all PAH species after pyrene were assumed to condense on the soot particle surface [37,50]. In this work, inception was assumed to occur by the dimerisation of two pyrene molecules and pyrene was assumed to be the only condensation species. This assumption is adequate for the flame studied considering the uncertainty in the aromatics chemistry and the fact that the concentration of PAHs having sizes larger than pyrene are expected to be substantially smaller than that of pyrene. In addition, particles are subjected to a size-dependent collision rate [62] and undergo surface growth reactions described by the HACA mechanism [37] and oxidation by O_2 and OH [61].

The diffusion coefficient of a particle of size 1 is [63]:

$$D_{p,1}=\frac{3}{2\rho}\left(1+\frac{\pi\alpha_T}{8}\right)^{-1}\left(\frac{\bar{W}k_BT}{2\pi N_A}\right)^{1/2}\frac{1}{d_1^2}, \tag{6}$$

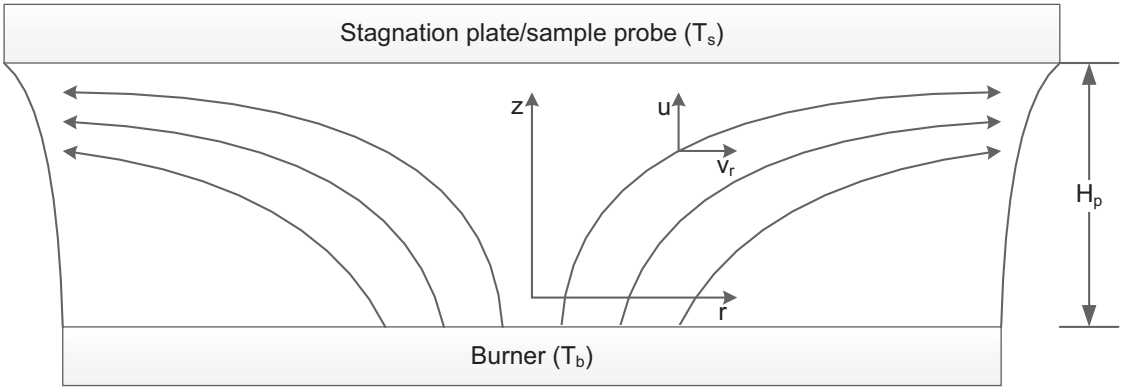

Fig. 1. Illustration of the coordinate system and the flow field in the burner-stabilised stagnation flame configuration. T is the temperature, H_p is the burner-stagnation plate separation, and u and v_r are the axial and radial velocities in the z and r directions, respectively.

where α_T (= 1.0) is the thermal accommodation factor which represents the equilibrium fraction of gas molecules that leave the particle surface, $\bar{W}$ is the mean molecular weight of the mixture, k_B is the Boltzmann constant, N_A is the Avogadro constant and d is the diameter. In the original Melton [64] work, a thermal accommodation factor of 0.9 was used. More recently, studies of laser-induced incandescence [65] used values around 0.3. In the present work, however, we found the results to be insensitive to α_T within this range.

The thermophoretic velocity may be expressed as [66]:

$$v_T = -\frac{3}{4}\left(1+\frac{\pi\alpha_T}{8}\right)^{-1}\frac{\mu}{\rho T}\frac{\mathrm{d}T}{\mathrm{d}z}, \tag{7}$$

where μ is the dynamic viscosity. A generalised theory for the transport of nano-sized particles was advanced by Li and Wang [67–69] where the transition from diffuse to specular scattering and van der Waals gas-particle interaction were accounted for. The influence of the improved diffusion and thermophoretic terms is to be investigated in future.

Boundary conditions

$$z=0: \quad U=\frac{\rho_b u_b}{2},\ G=0,\ T=T_b,\ \rho Y_k V_k=\rho u_b(Y_{k,b}-Y_k), \tag{8}$$

$$M_r=0, \tag{9}$$

where the value of U at the burner is based on the density and velocity of the feed. G, a variable related to the radial velocity, is zero because the radial velocity at the burner is assumed to be 0. T_b is the burner temperature and the species specification allows diffusion back into the burner.

$$z=H_p: \quad U=0,\ G=0,\ T=T_s,\ \rho Y_k V_k=0, \tag{10}$$

$$\frac{\partial v_T M_r}{\partial z}-\frac{\partial}{\partial z}\left[\rho D_{p,1}\frac{\partial}{\partial z}\left(\frac{M_{r-2/3}}{\rho}\right)\right]=0, \tag{11}$$

where H_p is the burner-stagnation plate separation, T_s is the plate temperature, and the boundary conditions for U, G and Y follow from a non-slip condition assumed at the plate.

It may be noted that Oppdif implements modified versions of Eqs. (4), (9) and (11) to solve for the natural logarithm of the moments because the values of the different moments may vary by several orders of magnitude. The moment boundary condition at the plate (Eq. (11)) was found to be well-approximated by a zero-gradient as there was no significant difference in the steady-state solution. It also resulted in a significant improvement in the convergence of the solution.

2.3. Detailed population balance model

A detailed population balance model [48] was used to model soot formation by postprocessing the Oppdif simulations of the BSSF. The growth of PAH species within the model is described by a kinetic Monte-Carlo-aromatic site (KMC-ARS) model [31], starting from pyrene. The dynamics of the soot particle population is described by the Smoluchowski equation [70–72] with additional terms for particle inception, surface growth, oxidation, condensation and sintering. A detailed description of the particle model [31,34,48] and the stochastic numerical method used to simulate the population dynamics [47,73] may be found elsewhere. A brief description of the most important aspects of the particle model is given below.

In the model, soot particles are represented as aggregates composed of primary particles, where each primary particle is composed of a number of PAHs [34]. A PAH is represented by the number of carbon and hydrogen atoms it contains, and the number and types of elementary sites on its edge [31]. These elementary sites include free-edge, zig-zag, armchair and bay sites [29,74]. This representation allows the exact structure and fringe length (defined as the largest carbon–carbon pair distance) of each individual PAH to be resolved. A primary particle is represented as a set of two or more PAHs. An aggregate is represented as a set of two or more primary particles. Each aggregate stores a list of neighbouring primary particles and resolves the shared surface area between each pair of neighbours, where each pair of neighbours can be in point contact, can be fully coalesced or can be anywhere in between [34]. The level of coalescence is described by a *sintering level* [41]. A sintering level of 0 corresponds to point contact and a sintering level of 1 corresponds to complete coalescence.

There are five different particle processes in the model:

Inception A primary particle is formed when two PAH molecules stick following a collision. The sticking probability of these two PAHs is determined by a simple collision efficiency model [48]. If the sum of the masses of the collision partners exceeds a given minimum particle inception size, then they will stick. This implies a unity sticking probability. The inception process in this part of the model is to be distinguished from the pre-processing step with Oppdif where pyrene dimerisation was assumed to be the inception process. Here we assume that a primary particle is formed when any two PAH molecules, pyrene or larger, stick following a collision.

Coagulation An aggregate is formed when two (primary or aggregate) particles stick following a collision. The rate of collision is determined by a transition regime coagulation kernel [47] which is dependent on the mass and collision diameter of each collision partner. After a coagulation event, two primary particles (one from each collision partner) are assumed to be in point contact. These primaries may undergo subsequent particle rounding due to mass addition [34] via surface growth and condensation, and due to sintering [41].

Surface growth PAHs in a primary particle may grow via surface reactions with gas-phase species. The rate of surface growth is a function of the structure of the PAH and is described by the KMC-ARS model. Two parameters are introduced to differentiate the rate of growth of PAHs in a primary particle versus those in the gas phase. The *growth factor* $g \in [0,1]$ [34] is a multiplier that is applied to the growth rate of PAHs within primary particles where the number of PAHs exceeds a critical number of PAHs, n_{crit}. It is intended to account for the possibility that PAHs in large primary particles grow more slowly than PAHs in the gas-phase.

Surface growth increases the mass of a PAH, which results in an increase in the sphericity of the primary particle containing the PAH and any neighbouring primary particles [34]. This particle rounding takes the form of an increase in the shared surface area between the affected primary particles. The rate of particle rounding is parameterised by a *smoothing factor* $s \in [0,2]$ [34] that relates the change of the shared surface area to the change of the volume of a primary particle. A smoothing factor of 0 implies instantaneous coalescence, whereas a smoothing factor of 2 corresponds to no rounding.

Condensation A particle may grow via condensation of a gas-phase PAH, following a collision between the PAH and a primary or aggregate particle. The rate of collision is calculated as per coagulation, except that one of the collision partners is a molecule. Rounding by mass addition occurs via the same mechanism as described for the surface growth process above.

Sintering Neighbouring primary particles may undergo particle rounding via a sintering process. The rate of sintering between each pair of neighbouring primary particles p_i and p_j is given [41]:

$$\frac{dC_{i,j}}{dt} = -\frac{1}{\tau_s}(C_{i,j} - S_{i,j}), \tag{12}$$

where $C_{i,j}$ is the shared surface area of primary particles p_i and p_j, and $S_{i,j}$ is the surface area of a sphere with the same volume as primaries p_i and p_j. The characteristic sintering time is given [75]:

$$\tau_s = A d_{i,j} \exp\left[\frac{E}{T}\left(1 - \frac{d_{crit}}{d_{i,j}}\right)\right], \tag{13}$$

where A is the pre-exponential factor, $d_{i,j}$ is the minimum diameter of two neighbouring primary particles, E is the activation energy and d_{crit} is the critical primary particle diameter below which the primaries are assumed to be liquid-like and 'sinter' instantaneously. It should be noted that a more physically-based relationship is desirable, for example one which could be characterised by the C/H ratio.

The sintering level $c_{i,j}$ determines how far primary particles p_i and p_j have sintered:

$$c_{i,j} = \frac{\frac{S_{i,j}}{C_{i,j}} - 2^{-1/3}}{1 - 2^{-1/3}}, \tag{14}$$

where a value of 0 implies that the primary particles are in point contact, while a value of 1 means that the primary particles are fully sintered.

There are many parameters in the model, but the key parameters investigated in this work are shown in Table 1. Ranges within which these parameters are expected to vary and the initial values chosen for the base case simulations are shown. The five parameters ρ, s, g, E and d_{crit} were optimised by Chen et al. [48] in a two-step process against the experimental PSDs for a set of laminar premixed ethylene flames [76].

3. Results and discussion

3.1. Temperature and species profiles

The centreline temperature for the stagnation flame in Fig. 1 was measured using a coated thermocouple [26] as a function of height above burner surface, H for six burner-stagnation plate separations, H_p = 0.55, 0.6, 0.7, 0.8, 1.0 and 1.2 cm. The top panel of Fig. 2 shows a comparison of the experimental and computed temperature profile for the largest burner-stagnation plate separation, H_p = 1.2 cm. The results are similar for the other separations. The size of the experimental error bars is due to the uncertainty (50–100%) in the emissivity of the thermocouple coating [26]. Also shown in Fig. 2 (bottom panel) is a comparison of the maximum

Table 1
Model parameters in detailed population balance model.

Parameter (units)	Range	Value
(1) Minimum particle inception size (number of carbon atoms)	Pyrene dimer 32 carbon atoms	Pyrene dimer 32 carbon atoms
(2) Soot density, ρ (g cm^{-3})	$1 \leqslant \rho \leqslant 2$	1.4
(3) Smoothing factor, s (–)	$0 \leqslant s \leqslant 2$	1.69
(4) Growth factor, g (–)	$0 \leqslant g \leqslant 1$	0.0263
(5) Critical number of PAHs in a primary particle before the growth factor is applied, n_{crit} (–)	$\geqslant 2$	50
(6) Sintering model:		
– A (s m^{-1})	N/A	1.1×10^{-14}
– E (K)	$1.8 \times 10^4 \leqslant E \leqslant 1.8 \times 10^5$	9.61×10^4
– d_{crit} (nm)	$1 \leqslant d_{crit} \leqslant 5$	1.58

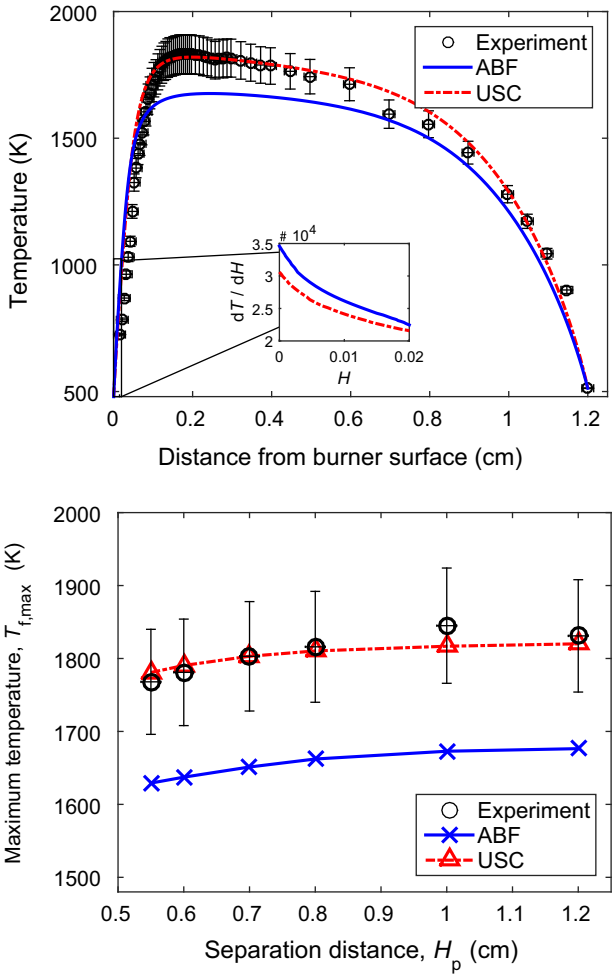

Fig. 2. Top panel: Comparison of experimental (symbols) and computed (solid line: ABF model; dashed-dotted-dashed line: USC Mech II) centreline temperature profiles for a burner-stagnation plate separation of 1.2 cm. Bottom panel: Comparison of experimental (symbols) and computed (solid line through symbols: ABF model; dashed-dotted-dashed line through symbols: USC Mech II) maximum flame temperatures at several burner-stagnation plate separations. The surface temperature (511 K) of the water cooled stagnation plate was used as a boundary condition for the simulation. The temperature was measured by a type-K thermocouple [26].

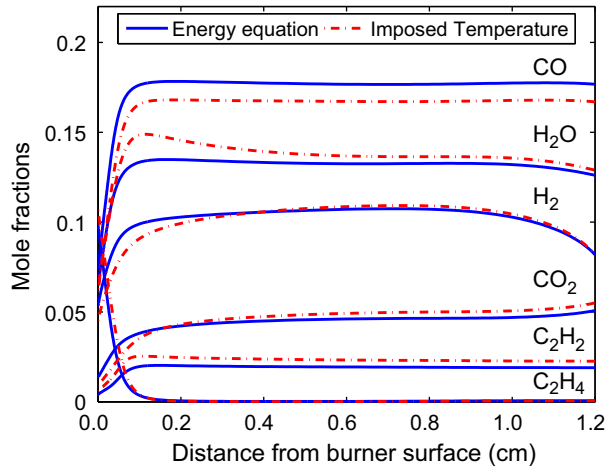

Fig. 3. Typical main species profiles computed for a burner-stagnation plate separation of 1.2 cm. Solid line: ABF model with energy equation solved; dashed-dotted-dashed lines: ABF model with experimental temperature profile imposed.

flame temperature for a range of separations. The maximum flame temperature increases with increasing separation due to the reduced conductive heat transfer to the stagnation plate as the burner to stagnation surface separation increases. Clearly the temperatures computed using the ABF model (solid lines) in the flame and postflame regions are as much as 150 K lower than the experimental value; and in the preheat zone the rise of the experimental temperature is slower than the computed results.

Previously, the same flame was simulated using USC Mech II [77]. The results show close agreement between the experimental and simulated temperature profiles for all H_p values. These simulations are repeated here with results also shown in Fig. 2. The inability of the ABF model to reproduce the temperature was puzzling initially, but it became clear to us that the flame chemistry part of the model over-predicts the laminar flame speed over the entire range of equivalence ratio, by as much as 30 cm/s (or over 100%) at the equivalence ratio of 1.8. The significantly larger flame speed leads to a faster rise in the temperature in the preheat zone, as seen in the inset in the top panel of Fig. 2, and thus a greater heat loss to the burner. At $H = 0.01$ cm, the temperature gradient is 2.6×10^4 K/cm for the ABF mechanism and 2.4×10^4 K/cm for USC Mech II. The result is a significantly reduced maximum flame temperature as seen in Fig. 2. The discrepancy of the experimental and simulated temperature is discerning, especially considering that the rate of soot formation is expected to be dependent on the temperature. As will be discussed later, we have carried out simulations both by solving the energy equation and by imposing the experimental temperature on the OPPDIF calculations. The difference in results will be discussed in detail.

Over almost the entire range of spatial distance of the postflame region, the concentrations of the major species are nearly constant, as shown in Fig. 3 for H_p = 1.2 cm as an example, except for H_2, which drops notably towards the stagnation surface. This is caused by the Soret effect: the sharp temperature gradient near the surface draws in heavier species. By continuity, the light species, e.g., H_2, must have a reduced concentration to compensate for

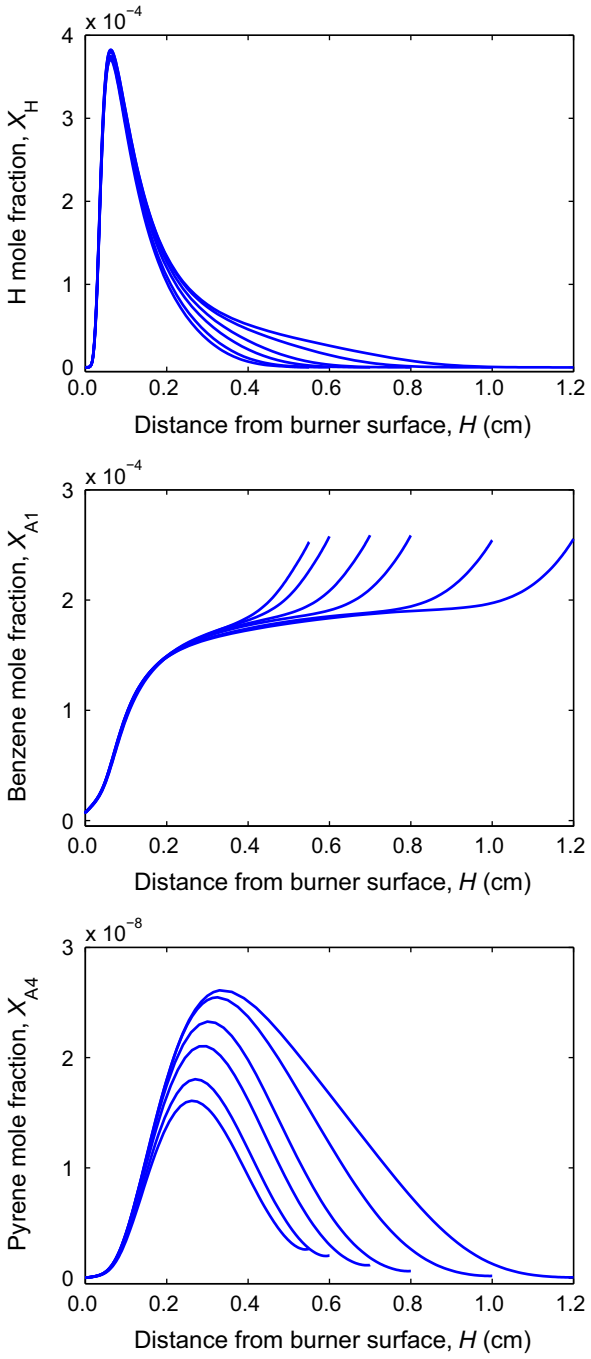

Fig. 4. Hydrogen atom, benzene and pyrene mole fraction profiles computed using the ABF model by solving the energy and other conservation equations for several burner-stagnation plate separations. Each curve corresponds to one plate position which is indicated by the value of H at the end of each curve.

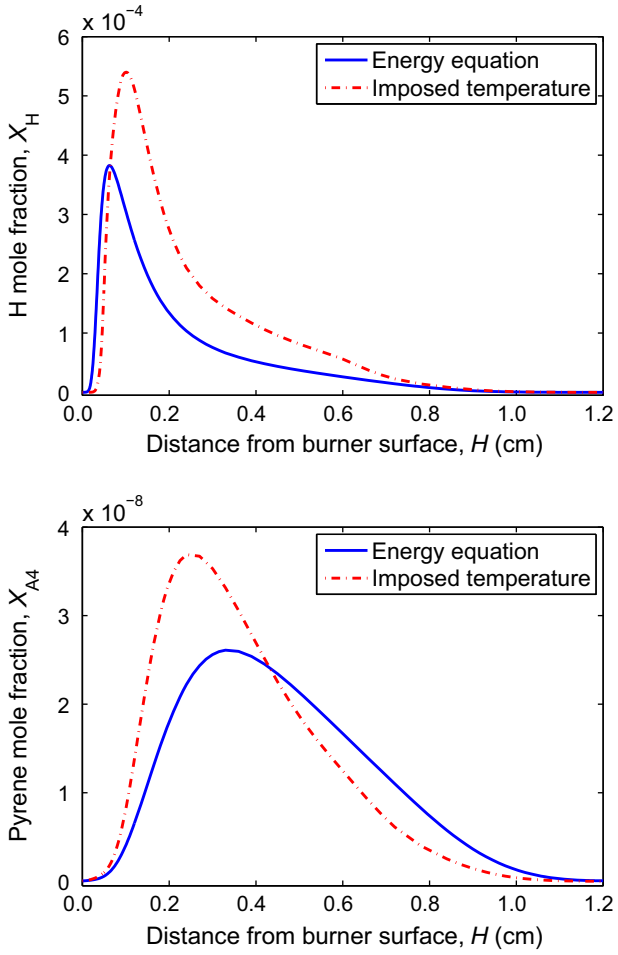

Fig. 5. Comparison of computed hydrogen atom (top panel) and pyrene (bottom panel) profiles where the energy equation was solved using the ABF model (with gas and particle radiation correction) and where the experimental temperature profile was imposed, both for a burner-stagnation plate separation of 1.2 cm.

the enrichment of the heavy species, as evidenced by the slight upward bending of the CO_2 mole fraction curve towards the stagnation surface. Figure 3 also shows major species profiles computed by imposing the experimental temperature profile without solving the energy equation. Overall, the temperature discrepancy causes small, but notable changes in the major species profiles.

Hydrogen atoms are critical to radical site generation in PAH molecules and soot surfaces [78]. Figure 4 shows the H atom, benzene and pyrene mole fraction profiles computed for a range of burner-stagnation plate separations. All three profiles show that the flames are very similar up to about 0.2 cm above the burner surface. The length of the post-flame region increases with increasing burner-stagnation plate separation.

Two types of PAH profiles have been observed in laminar sooting premixed flames [9,79–81]:

(1) In high temperature flames ($T_{f,\max} \gtrsim 1850$ K), concentrations would initially rise then fall in the post-flame region.

(2) In low temperature flames, concentrations would level off or continue to rise in the post-flame region.

The rise-then-fall behaviour has been explained to be the competition of PAH mass growth [52] and thermal decomposition [82]. We do not see the rise-then-fall in the benzene profiles here because these are a set of low temperature flames. However, we see a rise-then-fall in the profiles of pyrene because of its consumption from particle inception and condensation on soot surfaces.

The discrepancy for the temperature prediction by the base model has a notable impact on the H atom concentration and the prediction of precursors to soot. Figure 5 shows a comparison of the computed H atom and pyrene profiles where the energy equation was solved and where the experimental temperature profile was imposed at $H_p = 1.2$ cm. The higher temperatures imposed increases the H atom and peak pyrene concentration; however, it lowers the pyrene concentration in the post-flame region, for reasons to be discussed later.

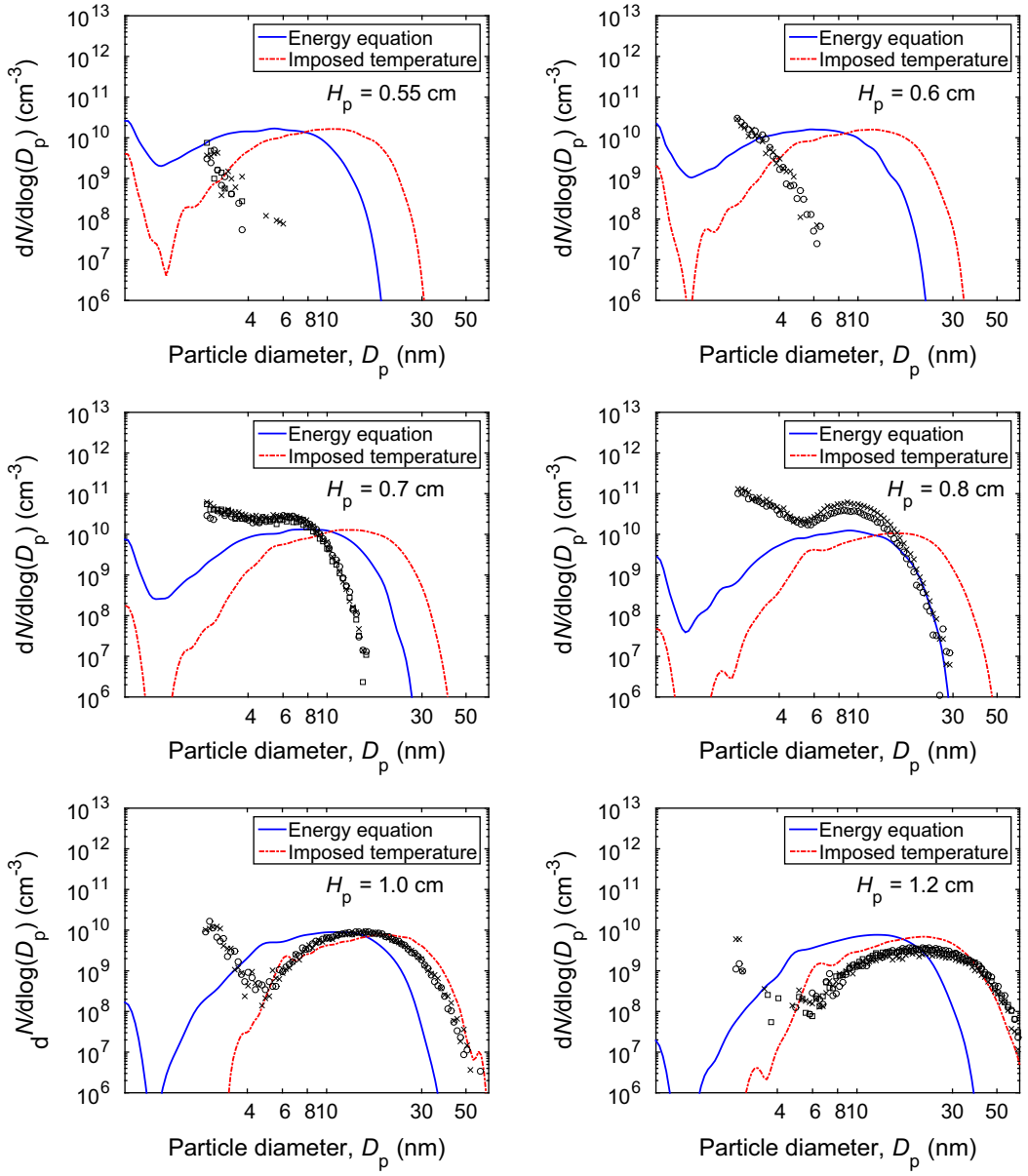

Fig. 6. Comparison of computed PSDs where the energy equation was solved (solid line) and where the experimental temperature profile was imposed (dashed-dotted-dashed line) at several burner-stagnation plate separations. Symbols are experimental data. Different symbols are used for different repeat experiments.

3.2. Particle size distributions

PSDs were determined by mobility diameter measurements and later compared with the particle sizes determined by HIM [17,19]. The inability to fully reconcile the PSDs highlights the need to model the mobility diameter which may aid in the interpretation of the mobility measurements.

We assume that the mobility diameter is equal to the collision diameter. While this is clearly an approximation [83], it has been employed in past modelling studies of laminar sooting flames (see, e.g., [84]). Regarding the basis for this assumption, we note the following. Nanoparticle transport theory in the large Knudsen number limit was used to determine a parameterised relationship between the physical size D_p and the mobility diameter $\widetilde{D}_p$ of a soot particle [35]. For the ratios between mobility and physical diameter, the values $D_p/\widetilde{D}_p = 0.8$, 0.94 and 0.98 for $\widetilde{D}_p = 3$, 10 and 20 nm, respectively, were found. Considering the uncertainties in present models, we conclude that a distinction between different types of diameter does not need to be made. (Theory is broadly applicable for Kn = 42, 13 and 6, respectively, for particles in air – atmospheric pressure and room temperature – with the same particle sizes $\widetilde{D}_p$ as above.)

PAHs and primary particles

The collision diameter is assumed here as:

$$d_c = \max\left(\left(\frac{6V}{\pi}\right)^{1/3}, d_A\left(\frac{2n_c}{3}\right)^{1/2}\right), \tag{15}$$

where the first term in the parenthesis corresponds to the equivalent spherical diameter while the second term corresponds to Frenklach's geometric relationship for the most condensed PAH series [61]. V is the "volume" of the PAH (or PAHs in the case of primary particles) calculated from the total mass of carbon and hydrogen atoms, and the density of soot material. d_A is the size of a single aromatic ring, equal to 1.395 $\sqrt{3}$ Å, or 2.42×10^{-10} m. n_c corresponds to the number of carbon atoms in a PAH. In light of the unknown mass density of the soot material when the particles are merely clusters of a few PAHs and the known non-sphericity of the primary particles [17,19], we expect Eq. (15) to be over-simplified.

Aggregates

The collision diameter follows the form of [85]:

$$d_c = d_p n_p^{1/D_f} = \frac{6V}{S}\left(\frac{S^3}{36\pi V^2}\right)^{1/D_f} = \frac{6}{(36\pi)^{1/D_f}}\frac{V^{1-2D_f}}{S^{3/D_f-1}}, \tag{16}$$

where d_p is the average primary particle diameter, n_p is the average number of primary particles in the aggregate, and D_f is the fractal dimension of soot particles (= 1.8). Note that in the case of surface-volume models which assume monodisperse, spherical primary particles in point contact, d_p and n_p represent the real primary particle diameter and number, respectively.

S is the surface area of the aggregate:

$$S = \frac{S_{\text{sph}}}{c_{\text{avg}}(1 - n^{-1/3}) + n^{-1/3}}, \tag{17}$$

where S_{sph} is the equivalent spherical surface area, c_{avg} is the average sintering level of the particle, and n is the number of primary particles. c_{avg} is calculated as the summation of all pairwise sintering levels in the particle (Eq. (14)) and averaged across the number of primary particle connectivities (or $n-1$). Eq. (17) interpolates between the surface area of a spherical particle ($c_{\text{avg}} = 1$) and the surface area of a particle where the primary particles are in point contact ($c_{\text{avg}} = 0$).

The predicted PSDs are found to be in qualitative agreement with the experimental data as shown in Fig. 6. In particular, the calculations where the energy equation was solved (hereon referred to as the base case) yield the bimodal distributions as observed experimentally. Quantitatively, however, the PSDs differ notably. There are three key aspects in the disagreement. First, the base case simulation yields onset of particle nucleation earlier than the experimental counterpart. For $H_p = 0.55$ cm, the experiment shows the first burst of small particles entering into the lower cutoff size of 2.5 nm, but computationally the model predicts substantially larger particles. This is to be expected since, computationally, the smallest particle is made up of two pyrene molecules, and experimentally the onset of particles is downstream of the peak pyrene mole fraction. Despite the earlier nucleation, however, the model predicts a smaller size growth rate. For example, at $H_p = 1.2$ cm, the model underpredicts the mean diameter of the large-size mode of particles by as much as a factor of 2. Lastly, the trough separating the two size modes was predicted to be deeper and smaller than the experiment. However, unlike the number density of the two size modes, the number density or depth of the trough has no physical significance as it is extremely sensitive to the bandwidth used for the kernel density function estimate of the PSD. The diameter associated with the trough is not sensitive to the bandwidth.

The discrepancy observed above is not entirely the consequence of temperature. As shown in Fig. 6, imposing the experimental temperature profile leads to an increase in the particle size as compared to the base case simulation. The increase in the predicted particle size is caused, to an extent, by the increased peak pyrene concentration, as seen in Fig. 5. Likewise, the larger soot surface area also leads to greater rates of pyrene consumption and a lowered pyrene concentration in the post flame. A consequence of the reduced pyrene concentration is a reduced nucleation intensity and a drop in the number density of the small-size mode, to the extent that the computed PSDs at the two largest burner-stagnation plate separations are unimodal. Overall, neither the base case simulation nor the run with imposed temperature reproduces the PSD data well. In what follows, we shall carry out sensitivity

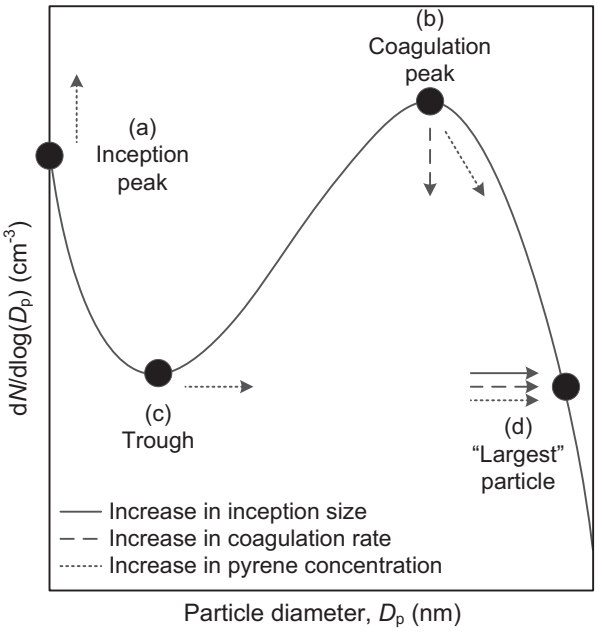

Fig. 7. Features of a bimodal PSD and summary of effects of the model parameters tested on the key features of the PSD.

analysis on the various model parameters to understand the plausible cause for the discrepancy.

3.3. Parametric sensitivity study

Key features of a bimodal PSD are identified for the purpose of making quantitative comparisons between the experimental and computed PSDs. Figure 7 shows these features: (a) a mode at small diameters (the inception peak) which represents incipient particles, (b) a mode at larger diameters (the coagulation peak) which represents particles that have grown by coagulation and surface growth, (c) a trough between these two modes and (d) the "largest" particle. Each feature has an associated number density and particle diameter D_p. Following the approach of [35], the diameter of the "largest" particle is defined to be the greatest diameter for which $dN/d\log(D_p) = 0.01N_{total}$, where N_{total} is the total number density. N_{total} is based on particle diameters $D_p > 2.5$ nm as the particle detection limit of the SMPS is 2.5 nm [26].

Key model parameters considered for sensitivity analysis are (a) the minimum particle inception size, (b) the particle–particle coagulation rate and (c) the pyrene concentration. The computation is carried out for $H_p = 1.2$ cm. Figure 8 shows the results of varying: (a) the minimum particle inception size, (b) the coagulation rate and (c) the pyrene concentration at $H_p = 1.2$ cm. To eliminate the uncertainty associated with the temperature prediction, the experimental temperature profile was imposed. Similar results were found for all other burner-stagnation plate separations ($H_p = 0.55$, 0.6, 0.7, 0.8 and 1.0 cm). The minimum particle inception size was varied from 32 carbon atoms (base case) to 1024 carbon atoms, and a constant multiplicative factor of 2, 4 and 8 was

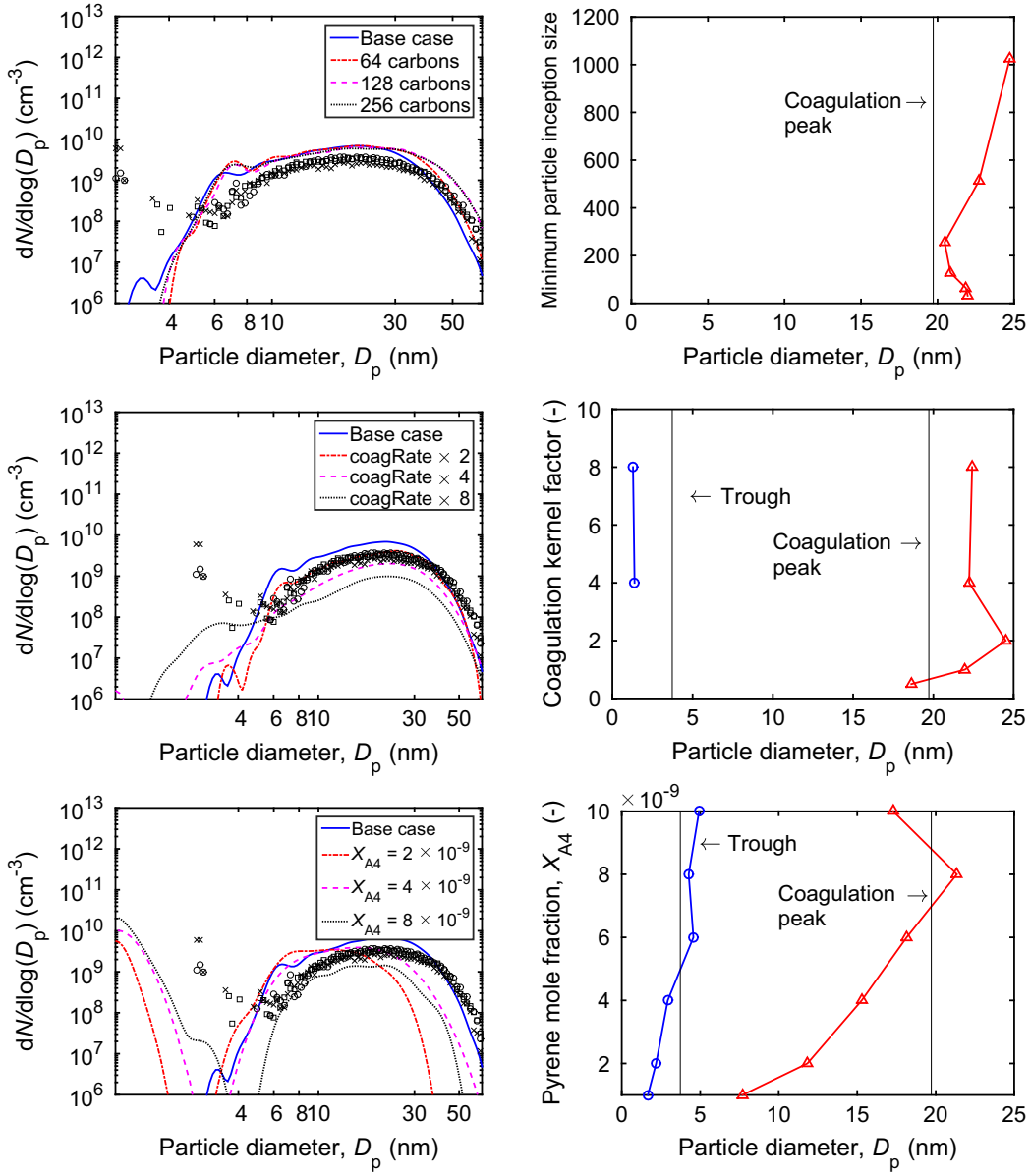

Fig. 8. Sensitivity of computed (lines) PSDs to the minimum particle inception size (top panel), the coagulation rate (middle panel) and the pyrene concentration (bottom panel) for a burner-stagnation plate separation of 1.2 cm where the experimental temperature profile was imposed. Left column: Symbols are experimental data. Different symbols are used for different repeat experiments. Right column: Sensitivity of the position of the trough between the modes of the bimodal PSD (circles) and the position of the coagulation peak (triangles). The vertical lines correspond to the experimental values for the trough (point c of Fig. 7) and coagulation peak (point b of Fig. 7).

applied to the coagulation kernel to assess the effect of changing the coagulation rate. There is an overall shift in the position of the coagulation peak to larger diameters. Increasing the minimum particle inception size increases the average size of PAHs in a particle. On the other hand, increasing the coagulation rate increases the number of coagulation events and therefore the number of PAHs in a particle. Both effects lead to an increase in particle diameter. A constant pyrene profile, i.e., the pyrene concentration does not change with height above burner, was imposed to understand the effect of precursor concentration on the various PSD features. Increasing the pyrene concentration leads to a systematic shift in both the position of the trough and the position of the coagulation peak to larger diameters, leading to a better agreement between the experimental and computed PSDs. Hence, it appears that the trough position is related to the precursor concentration or nucleation strength. We note, however, that these conclusions should be taken as preliminary due to the limited agreement between model and experiment.

The importance of precursor concentration in predicting the qualitative PSD features may be traced back to the theoretical study of Dobbins and Mulholland [86] who examined the evolution of the PSD for an aerosol undergoing simultaneous particle formation and coagulation; the diagrams of Pratsinis [87] which show the effects of chemical reaction, nucleation, condensation and coagulation on various aerosol characteristics, including the polydispersity of the aerosol; and detailed modeling of Frenklach, starting with [37,60], and providing a more in-depth analysis in [88–90].

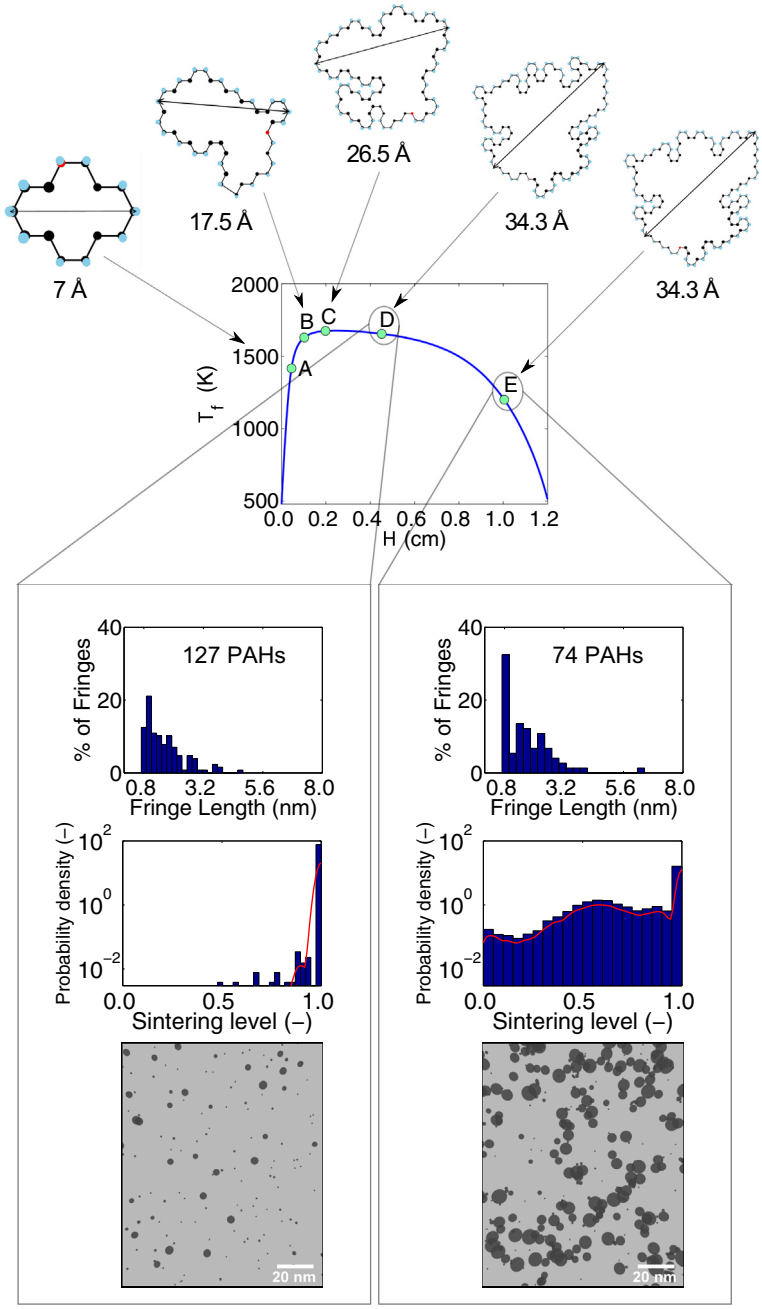

Fig. 9. Top panel: Evolution of the structure and fringe length of a representative PAH corresponding to points A–E on the temperature profile. Bottom panel (starting from the top): Fringe length distributions (the number of PAHs in the aggregate is shown), sintering level distributions and TEM images corresponding to points D and E on the temperature profile.

3.4. Soot morphology

Figure 9 shows various aspects of the soot morphology calculated from the detailed population balance model: (a) the evolution of the structure and fringe length of a representative PAH along the flame (top panel) and (b) computed fringe length distributions, sintering level distributions and computed, quasi-TEM images (bottom panel) in the post-flame region. The fringe length distribution corresponds to an aggregate which contains the largest (the number of carbon atoms) PAH at that point in the flame. The sintering level was calculated as an average for each aggregate in the particle ensemble and a distribution of these values are shown. In the TEM images, aggregates are represented as spheres in point contact.

Point D is a high temperature region just behind the flame front. The sintering level distribution and quasi-TEM image show that inception is dominant and almost all the particles in the ensemble are spherical. Point E is at a lower temperature near the stagnation plate. Incipient particles grow by coagulation and surface growth forming partially sintered aggregates. The sintering level distribution shows a peak at 1.0 corresponding to spherical particles, indicating that inception continues well into the post-flame region. Fringe length distributions show a peak at about 1 nm, with lengths ranging from 1 to 6 nm. The largest fringe length in either distribution corresponds to a PAH which starts growing from just above the burner surface. Fringe lengths at point E are on average larger than at point D because the residence time between these two points is relatively long. The computed fringe length distributions compare favourably with experimental observations made for a range of fuels [18].

If indeed the soot particles were spherical, no benefit would be gained from tracking the aggregate structure of the particles. However, HIM of nascent soot particles for a number of premixed ethylene BSSF show that these particles are neither spherical nor chain-like [17,19]. By imposing two different combinations of model parameters which result in two distinct soot morphologies this may help us to better interpret the mobility diameter. First of all, based on the parameters in Table 1, the model allows for the formation of polydisperse, sintered primary particles which is shown as the dashed-dotted-dashed line in Fig. 10. An infinitely fast sintering rate (large d_{crit}) and the instantaneous rounding of primary particles ($s = 0$) results in spherical particles. This model represents an oversimplification and results in an underprediction of the diameter associated with the coagulation peak (as indicated by the circles). Extending the basic spherical particle model to a surface-volume model by neglecting the sintering process and not accounting for the rounding of primary particles ($s = 2$) results in an overprediction of the diameter. This finding is expected to hold for both bimodal and unimodal PSDs. The inception peak in a bimodal PSD represents incipient particles which are spherical and all particle models effectively reduce to the spherical particle model. Menz and Kraft [28] demonstrated that under certain conditions, albeit in silica and silicon systems, all three models were equivalent to a spherical particle model. However, outside of this range, the spherical and surface-volume particle models were shown to incur substantial errors. In summary, this case study demonstrates that the prediction of the PSDs of an ensemble of polydisperse particles is dependent on the choice of the particle model. Where coagulation and sintering are significant the system is poorly described by spherical or surface-volume models.

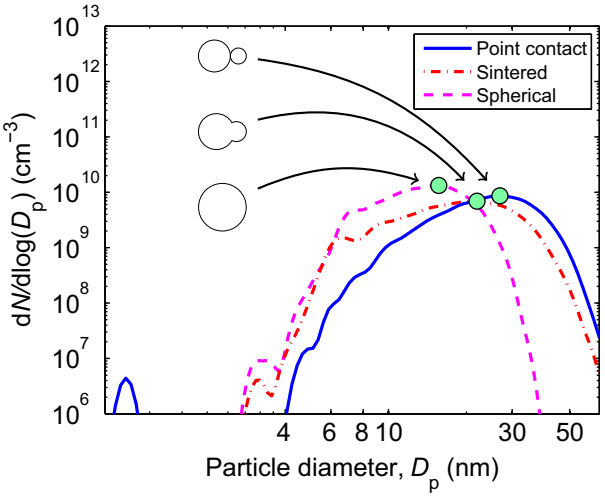

Fig. 10. Computed PSDs for a burner-stagnation plate separation of 1.2 cm with imposed experimental temperature profile for three different model cases: (1) polydisperse, spherical primary particles in point contact (continuous line), (2) polydisperse, sintered primary particles (dashed-dotted-dashed line) and (3) spherical particles (dashed line). The circles indicate the position of the coagulation peak.

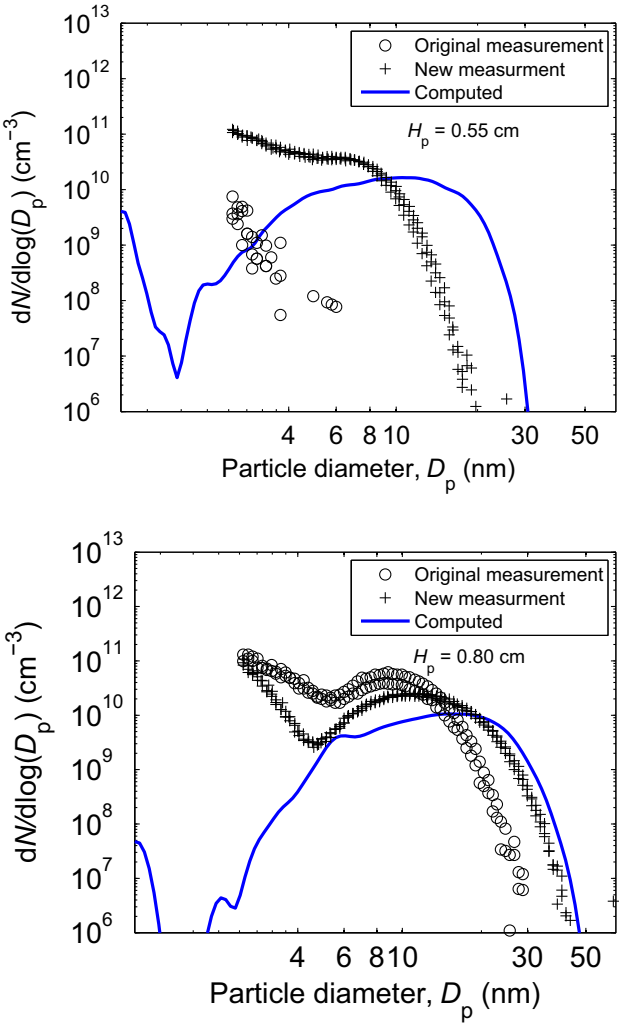

Fig. 11. Comparison of the original experimental measurement (circle symbol) reported in [26] with new measurement (plus sign) at different burner-stagnation plate separations. The new measurements are an attempt to reproduce the measurements in [26]. Computed PSDs (lines) where the experimental temperature profile was imposed are also shown.

4. Implications on mobility sizing experiments

Simulations carried out here cast some doubts about the accuracy of experimental data of Flame C3 [26]. Clearly, the exhaustive sensitivity analyses show that within the framework of the current model it would be difficult to reconcile the detailed features of the measured PSDs across all burner-probe separations and within a PSD from small to large particle sizes. There are several experimental issues that will require further scrutiny. First, the drastically different PSDFs for small burner-probe separations (see, Fig. 6) require the experiments to be revisited and repeated, especially to make sure that there are no facility/burner-dependent issues. Second, the disagreement in the PSDs can be a problem of mobility measurement.

Since the current paper was submitted, concerted efforts were made towards re-measurement of the PSDs for the C3 flame [91]. New measurements did not reveal any problem about the measured flame temperature, but they indeed reveal a problem with the original PSD data reported in [26], shown in Fig. 11 for burner-stagnation plate separations of 0.55 and 0.80 cm as examples. The new measurements were repeated at the Stanford facility as well as two other facilities using four different burners. Consistency amongst the three facilities despite differences in experimental setup gives us greater confidence in the new measurements. The onset of a bimodal PSD occurs even at the smallest separation of 0.55 cm. This leads to a PSD with a more mature coagulation mode – broader and characterised by larger particle diameters – at a larger separation of 0.80 cm. The new data bring a substantial better agreement with the model especially for small separations. The discrepancy between the old and new data may be attributed to changes of the local porosity of the porous plug in the old measurement, a problem that was not discovered until recently. Over time, the flow rate in the centre region of the burner can become smaller, leading to a lower centreline flame temperature [91].

Another finding of the recent measurement is that due to particle morphological factors, the mobility diameter and the spherical particle assumption overestimate the particle mass. Using a Couette centrifugal particle mass analyzer (CPMA) [92]: it was found [91] that the ratio of actual-to-estimated particle mass was 0.5–0.6 for particles in the size range of 20–25 nm, and $\sim$ 0.9 for smaller particles. Figure 12 shows the ratio of the particle mass to the mass of a spherical particle of the same collision diameter, computed for particles at burner-stagnation plate separations of 0.55, 0.7 and 1 cm. For particle diameters less than 10 nm, the ratio is about 0.8 and for larger particles in the size range of 20–25 nm, the ratio is about 0.4. These computed ratios are inline with the experimental measurement [91]. Hence, the remaining model-experiment discrepancy cannot be attributed to morphological factors.

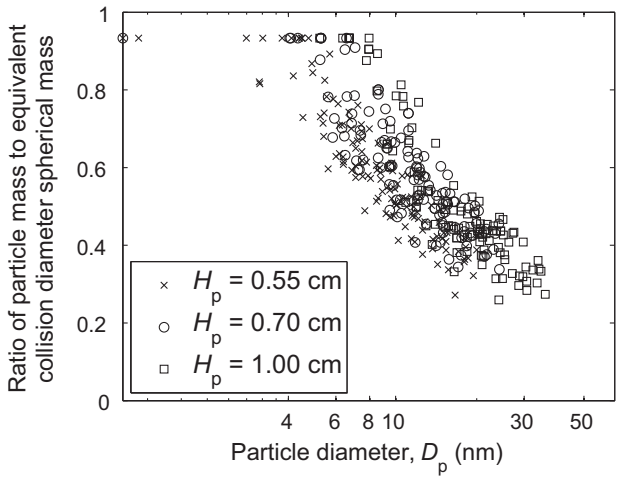

Fig. 12. Ratio of the computed particle mass to the mass of a spherical particle of the same collision diameter, computed for particles at different burner-stagnation plate separations. For primary particles represented as a set of two or more PAHs, the ratio is one. Whereas aggregates which are made up of two or more primary particles, the ratio will be less than one.

5. Conclusions

In this paper we have presented a modelling study of soot formation for a laminar premixed ethylene BSSF. A detailed population balance model was used to perform a parametric sensitivity study to understand the influence of the most important parameters on key features of the computed PSDs. We provided insight into soot formation through the analysis of computed sintering level distributions, fringe length distributions and TEM images.

The computed flame structure captured the trends in the experimental data, with temperatures reaching a maximum just above the burner surface. The computed minor species profiles were remarkably similar up to about 0.2 cm above the burner surface. The length of the post-flame region increases with increasing burner-stagnation plate separation.

We have illustrated a dependence of soot morphology upon flame conditions in the post-flame region. The computed particles are initially spherical, evolving to partially sintered aggregates. Computed fringe length distributions compare favourably with experimental distributions reported in the literature, with lengths ranging from 1 to 6 nm.

The base case simulations resulted in PSDs which overpredicted particle diameters at smaller separations and underpredicted particle diameters at larger separations. A parametric sensitivity study was performed to understand the cause of the discrepancies between the experimental and computed PSDs. The computed PSDs were found to be sensitive to the minimum particle inception size, the coagulation rate and the inception species concentration. Changes in the particle inception size and the coagulation rate led to an overall shift in the position of the coagulation peak. Only changes in the inception species concentration led to a systematic shift in both the position of the trough between the modes of the bimodal PSD and the coagulation peak at larger diameters. Given the overall model, varying the inception species concentration with each burner-stagnation plate separation was the only means possible of achieving a better agreement between the experimental and computed PSDs. Initiated by the questions raised through the current modeling study, new PSD measurements were made which went some way towards explaining the discrepancy between the experiment and model. In particular, the new measurement shows the onset of nucleation to be earlier than originally measured, thus bringing the modeling and experimental results closer to each other. However, the fact that the experimental PSDs could not be fully reconciled by the model within its current frame work suggests that a better understanding of the nucleation process, including the PAH precursor chemistry, is required before further progress can be made.

Acknowledgments

Discussions with Prof. M.J. Thomson, Dr. W.J. Menz and Mr. A.J. Smith were helpful in the direction of this work. Financial support by the Gates Cambridge is gratefully acknowledged. This project is partly funded by the National Research Foundation (NRF) – Singapore, Prime Minister's Office, Singapore under its Campus

for Research Excellence and Technological Enterprise (CREATE) programme. Professor Markus Kraft has been supported by the Weierstrass Institute for Applied Analysis and Stochastics.

References

[1] A. D'Anna, Proc. Combust. Inst. 32 (2009) 593–613.
[2] H. Wang, Proc. Combust. Inst. 33 (2011) 41–67.
[3] M.Y. Choi, G.W. Mulholland, A. Hamins, T. Kashiwagi, Combust. Flame 102 (1995) 161–169.
[4] C.R. Shaddix, K.C. Smyth, Combust. Flame 107 (1996) 418–452.
[5] H. Wang, B. Zhao, B. Wyslouzil, K. Streletzky, Proc. Combust. Inst. 29 (2002) 2749–2757.
[6] J.P. Hessler, S. Seifert, R.E. Winans, T.H. Fletcher, Faraday Discuss. 119 (2001) 395–407.
[7] C.S. McEnally, U.O. Köylü, L.D. Pfefferle, D.E. Rosner, Combust. Flame 109 (1997) 701–720.
[8] B. Zhao, Z. Yang, J. Wang, M.V. Johnston, H. Wang, Aerosol Sci. Technol. 37 (2003) 611–620.
[9] B. Zhao, Z. Yang, Z. Li, M.V. Johnston, H. Wang, Proc. Combust. Inst. 30 (2005) 1441–1448.
[10] B. Zhao, K. Uchikawa, H. Wang, Proc. Combust. Inst. 31 (2007) 851–860.
[11] M.M. Maricq, Combust. Flame 137 (2004) 340–350.
[12] M.M. Maricq, Combust. Flame 144 (2006) 730–743.
[13] L.A. Sgro, A. De Filippo, G. Lanzuolo, A. D'Alessio, Proc. Combust. Inst. 31 (2007) 631–638.
[14] R.A. Dobbins, R.A. Fletcher, H.-C. Chang, Combust. Flame 115 (1998) 285–298.
[15] Ü.Ö. Köylü, C.S. McEnally, D.E. Rosner, L.D. Pfefferle, Combust. Flame 110 (1997) 494–507.
[16] R. Puri, R.J. Santoro, K.C. Smyth, Combust. Flame 97 (1994) 125–144.
[17] M. Schenk, S. Lieb, H. Vieker, A. Beyer, A. Gölzhäuser, H. Wang, K. Kohse-Höinghaus, ChemPhysChem 14 (2013) 3248–3254.
[18] R.L. Vander Wal, A.J. Tomasek, Combust. Flame 134 (2003) 1–9.
[19] M. Schenk, S. Lieb, H. Vieker, A. Beyer, A. Gölzhäuser, H. Wang, K. Kohse-Höinghaus, Proc. Combust. Inst. 35 (2015) 1879–1886.
[20] R.A. Dobbins, R.A. Fletcher, W. Lu, Combust. Flame 100 (1995) 301–309.
[21] B. Öktem, M.P. Tolocka, B. Zhao, H. Wang, M.V. Johnston, Combust. Flame 142 (2005) 364–373.
[22] B. Zhao, Z. Yang, M.V. Johnston, H. Wang, A.S. Wexler, M. Balthasar, M. Kraft, Combust. Flame 133 (2003) 173–188.
[23] A.D. Abid, N. Heinz, E.D. Tolmachoff, D.J. Phares, C.S. Campbell, H. Wang, Combust. Flame 154 (2008) 775–788.
[24] A.D. Abid, E.D. Tolmachoff, D.J. Phares, H. Wang, Y. Liu, A. Laskin, Proc. Combust. Inst. 32 (2009) 681–688.
[25] L. Deng, A. Kempf, O. Hasemann, O.P. Korobeinichev, I. Wlokas, Combust. Flame 162 (2015) 1737–1747.
[26] A.D. Abid, J. Camacho, D.A. Sheen, H. Wang, Combust. Flame 156 (2009) 1862–1870.
[27] R.P. Lindstedt, B.B.O. Waldheim, Proc. Combust. Inst. 34 (2013) 1861–1868.
[28] W.J. Menz, M. Kraft, Aerosol Sci. Technol. 47 (2013) 734–745.
[29] M. Celnik, A. Raj, R. West, R. Patterson, M. Kraft, Combust. Flame 155 (2008) 161–180.
[30] M.S. Celnik, M. Sander, A. Raj, R.H. West, M. Kraft, Proc. Combust. Inst. 32 (2009) 639–646.
[31] A. Raj, M. Celnik, R. Shirley, M. Sander, R. Patterson, R. West, M. Kraft, Combust. Flame 156 (2009) 896–913.
[32] A. Raj, P.L.W. Man, T.S. Totton, M. Sander, R.A. Shirley, M. Kraft, Carbon 48 (2010) 319–332.
[33] A. Raj, M. Sander, V. Janardhanan, M. Kraft, Combust. Flame 157 (2010) 523–534.
[34] M. Sander, R.I.A. Patterson, A. Braumann, A. Raj, M. Kraft, Proc. Combust. Inst. 33 (2011) 675–683.
[35] J. Singh, R.I.A. Patterson, M. Kraft, H. Wang, Combust. Flame 145 (2006) 117–127.
[36] N. Morgan, M. Kraft, M. Balthasar, D. Wong, M. Frenklach, P. Mitchell, Proc. Combust. Inst. 31 (2007) 693–700.
[37] M. Frenklach, H. Wang, Proc. Combust. Inst. 23 (1990) 1559–1566.
[38] S. Mosbach, M.S. Celnik, A. Raj, M. Kraft, H.R. Zhang, S. Kubo, K.-O. Kim, Combust. Flame 156 (2009) 1156–1165.
[39] P. Lavvas, M. Sander, M. Kraft, H. Imanaka, Astrophys. J. 728 (2011) 80.
[40] R.H. West, R.A. Shirley, M. Kraft, C.F. Goldsmith, W.H. Green, Combust. Flame 156 (2009) 1764–1770.
[41] M. Sander, R.H. West, M.S. Celnik, M. Kraft, Aerosol Sci. Technol. 43 (2009) 978–989.
[42] W.J. Menz, M. Kraft, Combust. Flame 160 (2013) 947–958.
[43] A.E. Lutz, R.J. Kee, J.F. Grear, F.M. Rupley, OPPDIF: A FORTRAN Program for Computing Opposed-Flow Diffusion Flames, Sandia National Laboratories, Livermore, 1997.
[44] M.D. Smooke, I.K. Puri, K. Seshadri, Proc. Combust. Inst. 21 (1986) 1783–1792.
[45] K.L. Revzan, N.J. Brown, M. Frenklach. <http://www.me.berkeley.edu/soot>.
[46] J. Singh, M. Balthasar, M. Kraft, W. Wagner, Proc. Combust. Inst. 30 (2005) 1457–1465.
[47] R.I.A. Patterson, J. Singh, M. Balthasar, M. Kraft, W. Wagner, Combust. Flame 145 (2006) 638–642.
[48] D. Chen, Z. Zainuddin, E. Yapp, J. Akroyd, S. Mosbach, M. Kraft, Proc. Combust. Inst. 34 (2013) 1827–1835.
[49] J. Akroyd, A.J. Smith, R. Shirley, L.R. McGlashan, M. Kraft, Chem. Eng. Sci. 66 (2011) 3792–3805.
[50] J. Appel, H. Bockhorn, M. Frenklach, Combust. Flame 121 (2000) 122–136.
[51] CHEMKIN-PRO 15112, Reaction Design, San Diego, 2011.
[52] H. Wang, M. Frenklach, Combust. Flame 110 (1997) 173–221.
[53] R.J. Kee, J.A. Miller, G.H. Evans, G. Dixon-Lewis, Proc. Combust. Inst. 22 (1988) 1479–1494.
[54] H. Pitsch, E. Riesmeier, N. Peters, Combust. Sci. Technol. 158 (2000) 389–406.
[55] R. Siegel, J.R. Howell, Thermal Radiation Heat Transfer, McGraw-Hill, New York, 1972.
[56] C.L. Tien, S.C. Lee, Prog. Energy Combust. Sci. 8 (1982) 41–59.
[57] M.F. Modest, Radiative Heat Transfer, Academic Press, San Diego, 2003.
[58] K.C. Smyth, C.R. Shaddix, Combust. Flame 107 (1996) 314–320.
[59] D.R. Snelling, F. Liu, G.J. Smallwood, O.L. Gülder, Combust. Flame 136 (2004) 180–190.
[60] M. Frenklach, S.J. Harris, J. Colloid Interface Sci. 118 (1987) 252–261.
[61] M. Frenklach, H. Wang, in: H. Bockhorn (Ed.), Soot Formation in Combustion–Mechanisms and Models, Springer-Verlag, Berlin, 1994.
[62] M. Frenklach, Chem. Eng. Sci. 57 (2002) 2229–2239.
[63] P.S. Epstein, Phys. Rev. 23 (1924) 710–733.
[64] L.A. Melton, Appl. Opt. 23 (1984) 2201–2208.
[65] H.A. Michelsen, F. Liu, B.F. Kock, H. Bladh, A. Boiarciuc, M. Charwath, T. Dreier, R. Hadef, M. Hofmann, J. Reimann, S. Will, P.-E. Bengtsson, H. Bockhorn, F. Foucher, K.-P. Geigle, C. Mounaïm-Rousselle, C. Schulz, R. Stirn, B. Tribalet, R. Suntz, Appl. Phys. B 87 (2007) 503–521.
[66] L. Waldmann, K.H. Schmitt, in: C.N. Davies (Ed.), Aerosol Science, Academic Press, London, 1966.
[67] Z. Li, H. Wang, Phys. Rev. E 68 (2003) 061206.
[68] Z. Li, H. Wang, Phys. Rev. E 68 (2003) 061207.
[69] Z. Li, H. Wang, Phys. Rev. E 70 (2004) 021205.
[70] N.A. Fuchs, The Mechanics of Aerosols, Pergamon, Oxford, 1964.
[71] J.H. Seinfeld, S.N. Pandis, Atmospheric Chemistry and Physics–From Air Pollution to Climate Change, Wiley, New York, 1998.
[72] S.K. Friedlander, Smoke, Dust, and Haze, Wiley, New York, 1977.
[73] M. Celnik, R. Patterson, M. Kraft, W. Wagner, Combust. Flame 148 (2007) 158–176.
[74] M. Frenklach, Proc. Combust. Inst. 26 (1996) 2285–2293.
[75] S. Tsantilis, H. Briesen, S.E. Pratsinis, Aerosol Sci. Technol. 34 (2001) 237–246.
[76] J. Happold, Geschichtete polyzyklische aromatische Kohlenwasserstoffe als Bausteine der Rußbildung, Universität Stuttgart, Stuttgart, 2008.
[77] H. Wang, X. You, A.V. Joshi, S.G. Davis, A. Laskin, F. Egolfopoulos, C.K. Law, USC Mech Version II. High-Temperature Combustion Reaction Model of H2/CO/C1-C4 Compounds, 2007. <http://ignis.usc.edu/USC_Mech_II.htm/>.
[78] H. Wang, D.X. Du, C.J. Sung, C.K. Law, Proc. Combust. Inst. 26 (1996) 2359–2368.
[79] T.R. Melton, F. Inal, S.M. Senkan, Combust. Flame 121 (2000) 671–678.
[80] A. Ciajolo, A. D'Anna, R. Barbella, A. Tregrossi, A. Violi, Proc. Combust. Inst. 26 (1996) 2327–2333.
[81] A. El Bakali, X. Mercier, M. Wartel, F. Acevedo, I. Burns, L. Gasnot, J.-F. Pauwels, P. Desgroux, Energy 43 (2012) 73–84.
[82] M. Frenklach, J. Warnatz, Combust. Sci. Technol. 51 (1987) 265–283.
[83] C.M. Sorensen, Aerosol Sci. Technol. 45 (2011) 765–779.
[84] M.E. Mueller, G. Blanquart, H. Pitsch, Combust. Flame 156 (2009) 1143–1155.
[85] F.E. Kruis, K.A. Kusters, S.E. Pratsinis, B. Scarlett, Aerosol Sci. Technol. 19 (1993) 514–526.
[86] R.A. Dobbins, G.W. Mulholland, Combust. Sci. Technol. 40 (1984) 175–191.
[87] S.E. Pratsinis, J. Colloid Interface Sci. 124 (1988) 416–427.
[88] P. Mitchell, M. Frenklach, Proc. Combust. Inst. 27 (1998) 1507–1514.
[89] M. Balthasar, M. Frenklach, Combust. Flame 140 (2005) 130–145.
[90] M. Balthasar, M. Frenklach, Proc. Combust. Inst. 30 (2005) 1467–1475.
[91] J. Camacho, C. Liu, C. Gu, H. Lin, Z. Huang, Q. Tang, X. You, C. Saggese, Y. Li, H. Jung, L. Deng, I. Wlokas, H. Wang, Combust. Flame (2015) (in preparation).
[92] J.S. Olfert, N. Collings, J. Aerosol Sci. 36 (2005) 1338–1352.